Numerical Analysis of Sloshing and Wave Breaking in a Small Vessel by CIP-LSM*

Takehiro HIMENO**, Toshinori WATANABE**, Satoshi NONAKA***, Yoshihiro NARUO*** and Yoshifumi INATANI***

For the prediction of sloshing in the propellant tank of a rocket vehicle, the preliminary investigation was conducted. The flow field in the propellant tank during the ballistic flight of the vehicle was experimentally reproduced with the sub-scale model. The lateral acceleration as large as about 0.8 G was provided with a mechanical exciter and the deformation of the liquid surface in the small vessel was visualized with a high-speed camera. The sloshing phenomena were also simulated with the CFD code, called CIP-LSM. The important features of surface deformation and wave breaking were successfully reproduced in the computation.

***Key Words*:** Propellant Management, Sloshing, Wave Breaking, CIP, Level Set, MARS

1. Introduction

With the progress of human activities in space, the occasion to handle liquids under low gravity conditions is now growing. In weightless flights, the absence or diminution of gravity force makes it extremely difficult to position and control two-phase fluids in a desirable manner. For the establishment of the technology for the management of fluid or liquid propellant[(1)] in space, it is essential to accumulate technical knowledge to enable appropriate assessment of the fluid systems designed for space applications. However, in the atmosphere, there are not so many opportunities to realize the low-gravity state with airplanes or drop towers. Investigative methods based on CFD, Computational Fluid Dynamics, are therefore strongly desired.

2. Background

Figure 1 shows the flight of a rocket vehicle conducted by ISAS/JAXA, the Institute of Space and Astronautical Science. In the series of the reusable rocket vehicle testing, RVT[(2)], vertical landing, repeated flight capabilities and turnaround characteristics were demonstrated.

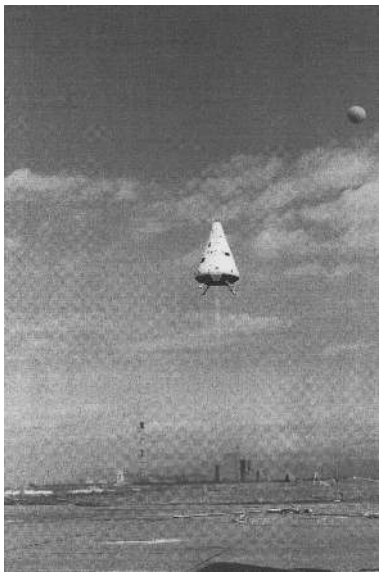

Fig. 1 Reusable rocket Vehicle Testing (RVT), conducted by ISAS/JAXA at Noshiro Testing Center in 2003.

The liquid hydrogen-propelled vehicle, shown in Fig. 2, was designed to provide opportunities for the studies and investigations on the technical issues aimed at the realization of reusable launch vehicle (RLV) in the future, such as flight on demand, quick turnaround, higher performance, light weight structures and materials and so on. The performance of the test vehicle at present is still limited. However, many lessons were learned and more flights will be conducted to improve the performance of the hardware and software through flight operations.

* Received 28th April, 2004 (No. 04-4092)

** Department of Aeronautics and Astronautics, University of Tokyo, 7–3–1 Hongo, Bunkyo-ku, Tokyo 113–8656, Japan.
E-mail: himeno@aero.t.u-tokyo.ac.jp

*** Institute of Space and Astronautical Science, Japan Aerospace Exploration Agency, 3–1–1 Yoshinodai, Sagamihara-shi, Kanagawa 229–8510, Japan

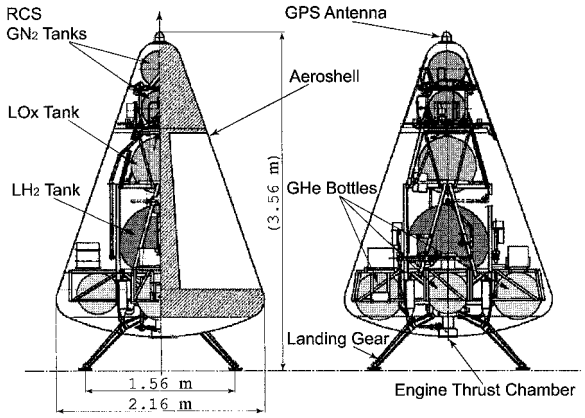

Fig. 2 Perspective drawing of the test vehicle which utilizes LOX and LH_2 as propellants for the pressure-fed-type engine

The propulsion system of the test vehicle acquires the capability of re-ignition, which enables the rocket engine to burn more than two times during the flight. It is not only a minimum requirement for achieving vertical landing after the ballistic flight, but also enables various sequences such as those in sounding missions or aborting operations. Indeed, the possibility of the ballistic flight followed by the re-ignition at low altitude is considered for the future campaign of RVT.

Nevertheless, from the viewpoint of the propellant management, it becomes very difficult to maintain the liquid propellant at the desirable position in the tank under the low-gravity condition during the ballistic flight. During this period, the vertical acceleration by aerodynamic force can be as small as 0.01 G, whereas the lateral acceleration can be a level similar to the lateral one induced by the side wind with a speed of 5 meters per second. Hence, there is concern that the high amplitude sloshing of liquid propellant might take place in the tank. If a large amount of gaseous helium, which is utilized for pressurization, should be sucked out through the outlet port located at the bottom of the tank and reach the combustion chamber, it might lead to failure of the re-ignition sequence and, in the worst case scenario, the loss of the vehicle.

3. CIP-LSM: Numerical Method for Free-Surface Flow

To establish the fundamental technology for propellant management in space transportation systems, a numerical method, called CIP-LSM[3]–[5], is under development to simulate three-dimensional free-surface flows under various gravity conditions. In the present paper, the experimentally observed flow fields were numerically simulated with the code and the computed results were compared with the experimental data for validation.

3.1 Governing equations

In this method, no-slip velocity is assumed between the vapor phase and liquid phase. Both the gaseous and liquid flows are described by three-dimensional Navier-Stokes equations for homogeneous two-phase flow as follows;

$$\frac{\partial \rho}{\partial t} + (\vec{u}\cdot\nabla)\rho = -\rho\nabla\cdot\vec{u} \tag{1}$$

$$\rho\frac{\partial \vec{u}}{\partial t} + \rho(\vec{u}\cdot\nabla)\vec{u} = \nabla:\mathbf{\Pi} + \vec{g} \tag{2}$$

$$\rho\frac{\partial e}{\partial t} + \rho(\vec{u}\cdot\nabla)\,e = \{\mathbf{\Pi}:\nabla\}\cdot\vec{u} - \nabla\cdot\vec{q}, \tag{3}$$

where the stress tensor Π includes the tensors of pressure $p\boldsymbol{I}$, viscous force $\boldsymbol{T}_v$ and surface force $\boldsymbol{T}_\sigma$. With the unit vector $\vec{n}_S$ perpendicular to the liquid surface, each tensor is written as

$$\Pi = -p\boldsymbol{I} + \boldsymbol{T}_v + \boldsymbol{T}_\sigma \tag{4}$$

$$\boldsymbol{T}_v = \lambda(\nabla\cdot\vec{u})\,\boldsymbol{I} + \mu(\nabla\vec{u} + \nabla\vec{u}^T) \tag{5}$$

$$\boldsymbol{T}_\sigma = \sigma\delta_S(\boldsymbol{I} - \vec{n}_S\vec{n}_S). \tag{6}$$

In CIP-LSM, the governing equations are described and discretized along the generalized curved coordinates (ξ,η,ζ), and the independent variables $\vec{Q} = (T, p, \vec{u})^T$ are solved with TCUP[3]–[6], temperature-based CCUP[7]. In the discretization, the variables $\vec{Q}$ are collocated at the center of each control volume Ω, where

$$\Omega = \{(x,y,z)|i-1/2\le\xi\le i+1/2, j-1/2\le\eta\le j+1/2, \\ k-1/2\le\zeta\le k+1/2\}. \tag{7}$$

and the Jacobian and metrics are evaluated in terms of the volume and the surface area of Ω, respectively. The algorithm of TCUP is schematically illustrated and summarized in Fig. 3 and Table 1.

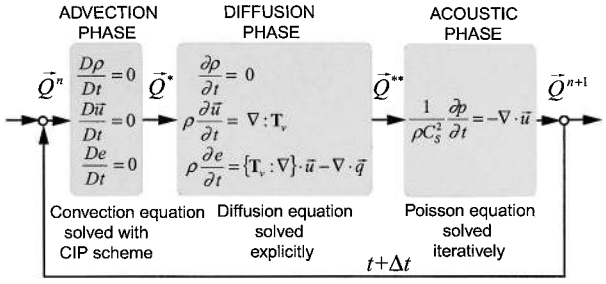

Fig. 3 Algorithm of CCUP scheme

3.2 Tracking surface position

In order to track the motion of the liquid surface and capture the configuration, the hybrid algorithm, called HLSM[4], was developed on the basis of the LSM[8],[9] and MARS[10]. In this method, to specify the attribution of phase state, vapor or liquid, on the fixed grid system, the Heaviside function $H_S(\xi,\eta,\zeta)$ is introduced as an independent variable and is defined as follows;

$$\begin{aligned} &H_S = 0.5 : \text{where the fluid attributes to the liquid state,}\\ &H_S = 0 : \text{the point locates on the liquid surface,}\\ &H_S = -0.5 : \text{where the fluid attributes to the vapor state.} \end{aligned} \tag{8}$$

Table 1 Algorithm of TCUP (Temperature-based CCUP)

·**Variant**	$: \vec{Q} = (T, p, \vec{u})^T$
·**Advection Phase**	$: \vec{Q}^n \rightarrow \vec{Q}^*$
$\vec{Q}$	$\dfrac{\partial \vec{Q}}{\partial t} + U_C^n \dfrac{\partial \vec{Q}}{\partial \xi} + V_C^n \dfrac{\partial \vec{Q}}{\partial \eta} + W_C^n \dfrac{\partial \vec{Q}}{\partial \zeta} = \vec{0}$
·**Diffusion Phase**	$: \vec{Q}^* \rightarrow \vec{Q}^{**}$
$\vec{u}$	$\displaystyle\int_\Omega \rho^* \frac{\vec{u}^{**} - \vec{u}^*}{\Delta t} dV = \int_{\partial\Omega} \mathbf{T}_v^* : d\vec{S}$
T	$\dfrac{T^{**} - T^*}{\Delta t} = \dfrac{\gamma^*}{(\rho C_p)^*} \dot{\Theta}$
p	$\dfrac{p^{**} - p^*}{\Delta t} = \dfrac{\gamma^* - 1}{(1 + \rho C_p \mu_J)^*} \dot{\Theta}$
·**Acoustic Phase**	$: \vec{Q}^{**} \rightarrow \vec{Q}^{n+1}$
p	$\displaystyle\int_\Omega \frac{p^{n+1} - p^{**}}{(\rho C_S^2)^{**} \Delta t} dV = -\int_{\partial\Omega} (\vec{u}^{**} - \frac{\nabla p^{n+1}}{\rho^{**}} \Delta t) \cdot d\vec{S}$
$\vec{u}$	$\dfrac{\Delta U_C}{J} = \left(-\dfrac{\nabla p^{n+1}}{\rho_m^{**}} + \vec{g} \right) \cdot \dfrac{\nabla \xi}{J} \Delta t$
T	$T^{n+1} - T^{**} = \dfrac{(1 + \rho C_p \mu_J)^{**}}{(\rho C_p)^{**}} (p^{n+1} - p^{**})$

The delta function in Eq. (6) can be written as

$$\delta_S \vec{n}_S = \nabla H_S . \tag{9}$$

Since neither condensation nor vaporization is considered in the present paper, the change of H_S in the flow field is described by the convection equation;

$$\frac{\partial H_S}{\partial t} + \nabla \cdot (H_S \vec{u}) = H_S \nabla \cdot \vec{u}. \tag{10}$$

This equation is solved by MARS[10], the Multi-interface Advection and Reconstruction Solver, which is PLIC[11]-like VOF[12] based algorithm proposed by Kunugi. By the spatial integration within Ω, Eq. (10) is discretized as follows;

$$\frac{H_V^{\#} - H_V^n}{J} = -\left\{ \sum_{\hat{\xi}=\xi,\eta,\zeta} [G_{\hat{\xi}}]_{-1/2}^{+1/2} \right\} \Delta t \tag{11}$$

$$\frac{H_V^{n+1} - H_V^{\#}}{J} = \left\{ \sum_{\hat{U}_C = U_C, V_C, W_C} \left[\frac{\hat{U}_C^{n+1}}{J} \right]_{-1/2}^{+1/2} \right\} H_V^n \Delta t, \tag{12}$$

where H_V denotes the volume fraction defined as

$$\frac{H_V}{J} = \int_\Omega H_S dV = \int_{k-1/2}^{k+1/2} \int_{j-1/2}^{j+1/2} \int_{i-1/2}^{i+1/2} H_S \frac{d\xi d\eta d\zeta}{J}, \tag{13}$$

and $G_{\hat{\xi}}$ represents the flux of H_V through each surface on Ω. The contravariant velocities are calculated from the physical velocities obtained after the operation of the acoustic phase in TCUP. Hence the position of the liquid surface is implicitly expressed and tracked indirectly as the contour of $H_V = 0$ in the fixed grid system.

For instance, flux G_ξ in the ξ-direction is calculated as follows. At first, the area fraction H_ξ on the intersection of Ω and the contour of ξ, is defined as

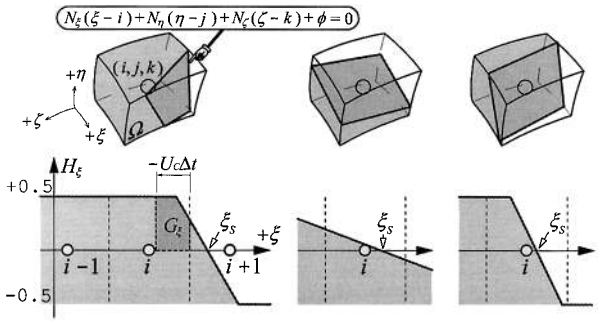

(a) $|\bar{\xi}| \geq |(|H'_\xi|^{-1} - 1)/2|$ (b) $|\bar{\xi}| < |(|H'_\xi|^{-1} - 1)/2|$

Fig. 4 Tangential plane of zero level set and the interpolation of H_ξ in ξ-direction based on MARS

$$\frac{H_\xi}{J} = \lim_{\Delta\xi \to 0} \left\{ \frac{1}{\Delta\xi} \int_{k-1/2}^{k+1/2} \int_{j-1/2}^{j+1/2} \int_{\xi-\Delta\xi/2}^{\xi+\Delta\xi/2} H_S \frac{d\xi d\eta d\zeta}{J} \right\}. \tag{14}$$

Then, the profile of H_ξ within $|\xi - i| \leq 1/2$ is interpolated with a piecewise linear function as Eq. (15).

$$H_\xi = \max\{-0.5, \min[0.5, H'_\xi(\xi - \xi_S)]\} \tag{15}$$

As shown in Fig. 4, when Ω intersects the liquid surface, the tangential plane at the nearest point on the liquid surface from the corresponding grid point in the Ω is written as

$$N_\xi(\xi - i) + N_\eta(\eta - j) + N_\zeta(\zeta - k) + \phi = 0, \tag{16}$$

where ϕ represents the signed distance from the liquid surface in the physical space, which will be defined as the 'level set function' later. The metrics being frozen in Ω, the coefficients in Eq. (16) can be described as

$$N_{\hat{\xi}} = (x_{\hat{\xi}}, y_{\hat{\xi}}, z_{\hat{\xi}}) \cdot \vec{n}_S \quad \text{for} \quad \hat{\xi} = \xi, \eta, \zeta, \tag{17}$$

and the inclination H'_ξ in the interpolated profile can be approximated as

$$H'_\xi = N_\xi \Big/ \sqrt{N_\eta^2 + N_\zeta^2} . \tag{18}$$

Then, to satisfy the condition that the integral of H_ξ within $|\xi - i| \leq 1/2$ should correspond to H_V, the intercept ξ_S is given as follows;

$$\xi_S - i = \mathrm{sgn}(\bar{\xi}) \cdot \left\{ \left(|H'_\xi|^{-1} + 1 \right) \Big/ 2 - \sqrt{|H'_\xi|^{-1} - 2|\bar{\xi}|} \right\}$$
$$\left(\text{if} |\bar{\xi}| \geq \left| \left(|H'_\xi|^{-1} - 1 \right) \Big/ 2 \right| \right) \tag{19}$$

$$\xi_S - i = \bar{\xi} \cdot \min\left(1, |H'_\xi|\right)$$
$$\left(\text{if} |\bar{\xi}| < \left| \left(|H'_\xi|^{-1} - 1 \right) \Big/ 2 \right| \right) \tag{20}$$

where $\bar{\xi} = -H_V / H'_\xi$. (21)

After that, the trapezium integration of H_ξ in the upwind direction yields the value of flux G_ξ at $(\xi - i) = \pm 1/2$.

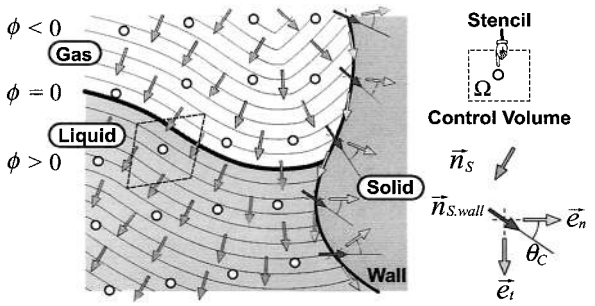

Fig. 5 Normal vector $\vec{n}_S$ and curvature κ of interface calculated from the distribution of ϕ.

$$G_\xi = \int_{(i\pm1/2)-U_C\Delta t}^{i\pm1/2} \frac{H_\xi}{J} d\xi \fallingdotseq \left\{ \int_{(i\pm1/2)-U_C^{n+1}\Delta t}^{i\pm1/2} H_\xi d\xi \Big/ U_C^{n+1}\Delta t \right\} \cdot \left(\frac{U_C^{n+1}}{J} \right) \Delta t. \quad (22)$$

With fluxes G_η and G_ζ evaluated in the same manner, the change of H_V can be obtained by Eqs. (11) and (12). Since the fluxes of H_V are given by the integration of the interpolated profile with the piecewise linear function, the dissipation of the liquid surface can be avoided distinctly and, at the same time, the volume conservation can be highly satisfied on the basis of the finite volume method. It is important that, by using ϕ for the calculation of H'_ξ, MARS is easily extended to the computation in the three-dimensional curved coordinate system.

3.3 Capturing surface configuration

In order to obtain the information on the surface configuration, the level set function ϕ is introduced as a dependent variable. As shown in Fig. 5, if ϕ remains the property of the distance function in terms of the liquid surface, i.e.,

$$|\nabla\phi| = 1 \quad \text{in the flow field near the liquid surface,} \quad (23)$$

$$\text{and} \quad \phi = 0 \quad \text{on the liquid surface where } H_S = 0, \quad (24)$$

the normal vector $\vec{n}_S$ and the curvature κ of a ϕ- contour can be easily calculated from the spatial distribution by

$$\vec{n}_S = \frac{\nabla\phi}{|\nabla\phi|}, \quad \kappa = \nabla\cdot\vec{n}_S. \quad (25)$$

To realize property (23), the Hamilton-Jacobi type equation

$$\frac{\partial\phi}{\partial\tilde{t}} + (S_{LSM}\vec{n}_S)\cdot\nabla\phi = S_{LSM}, \quad (26)$$

$$\text{where} \quad S_{LSM} = \frac{\phi}{\sqrt{\phi^2 + (\varepsilon/2)^2}}, \quad (27)$$

is iteratively solved and the distribution of ϕ is re-initialized at every time step, as has been proposed by Sussman and Osher in the algorithm of LSM, Level Set Method[8,9], where $\tilde{t}$ represents virtual time for the iteration. By the application of CIP[13,14] to solve the left-hand-side of Eq. (26), LSM can also be easily extended to the curved coordinate system[4].

In the present mentioned CIP-LSM, to realize property (23) more explicitly, the condition

$$\phi = H_V \cdot \sqrt{N_\xi^2 + N_\eta^2 + N_\zeta^2} \quad \text{and} \quad S_{LSM} = 0 \quad \text{if} \quad |H_V| < 0.30 \quad (28)$$

is additionally imposed to Eq. (26). It is important that H_V is used in the re-initialization so that error in the volume conservation would not be accumulated.

Thus, owing to the complementary combination of MARS and LSM, HLSM can be used not only to advect the volume fraction adequately, but also to capture the deformation of the liquid surface distinctly.

3.4 Extended surface

In accordance with the original LSM, the extended Heaviside function H_ε is defined also in CIP-LSM as

$$H_\varepsilon = 0.5\cdot\max\left[-1.0, \min\left\{1.0, \frac{\phi}{\varepsilon} + \frac{1}{\pi}\sin\left(\frac{\pi\phi}{\varepsilon}\right)\right\}\right]. \quad (29)$$

Then, so as to relax the discontinuity and stabilize the difference computation, the physical properties at an arbitrary grid point, such as ρ and μ, are expressed as

$$\rho = 0.5(\rho_{Liq} + \rho_{Gas}) + H_\varepsilon(\rho_{Liq} - \rho_{Gas}), \quad (30)$$

where ρ_{Liq} and ρ_{Gas} are respectively calculated by the equations of state for monophase fluid as a function of p and T:

$$\rho_{Liq} = f_{Liq}(p,T), \quad \rho_{Gas} = f_{Gas}(p,T). \quad (31)$$

The other properties needed in TCUP are also given by the weighted averages as

$$X = (0.5 + H_\varepsilon)X_{Liq} + (0.5 - H_\varepsilon)X_{Gas}. \quad (32)$$

The forms of X for the various properties are listed in Table 2.

Table 2 Physical properties in transient zone: X in Eq. (32)

	Physical Properties	X
ρ	: Density	ρ
C_p	: Specific Heat at Constant p	ρC_p
C_v	: Specific Heat at Constant ρ	ρC_v
C_S	: Sound Velocity	$(\rho C_S^2)^{-1}$
μ_J	: Joule Thomson Coefficient	$\rho C_p \mu_J$
μ	: Viscosity Coefficient	μ^{-1}
k	: Heat Conductivity	k^{-1}

Figure 6 shows the translation between ϕ and H_ε and the illustration of their contours in the flow field around a rising bubble. Thus, the liquid surface is extended as a transient zone with the thickness of 2 ε.

Then, according to the CSF (Continuum Surface Force) model[12], the surface force appearing in the right-hand-side of Eq. (2) can be adequately estimated, as follows;

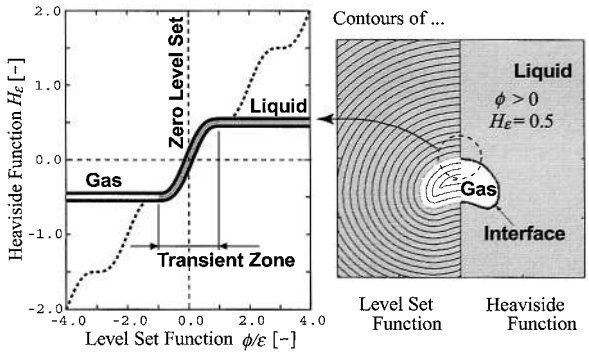

Fig. 6 Translation between H_ε and ϕ defined in the flow field around a rising bubble

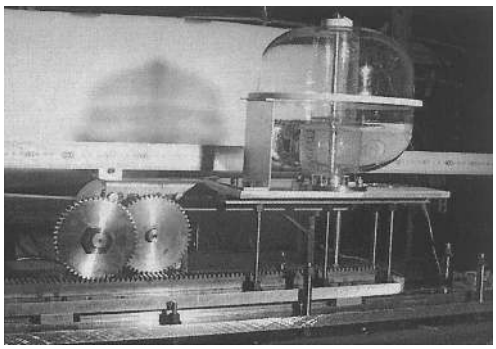

Fig. 7 The model tank mounted on the mechanical exciter.

$$\nabla : \boldsymbol{T}_\sigma = -\sigma\kappa\frac{dH_\varepsilon}{d\phi}\vec{n}_S = -\sigma\left\{\nabla\cdot\left(\frac{\nabla\phi}{|\nabla\phi|}\right)\right\}\frac{\nabla H_\varepsilon}{|\nabla\phi|}, \quad (33)$$

where surface tension σ is assumed to be constant.

4. Assessment of Liquid Behavior

In order to give appropriate assessment on the dynamic behavior of liquid propellant during ballistic flight, the sloshing motion in a small vessel was experimentally investigated. The second purpose of the experiment was to obtain the visualized data for checking the correlation with the numerical results.

4.1 Experimental assessment

Figure 7 shows the mechanical exciter manufactured for the present experiment, which was composed of a stepping motor, a rack-and-pinion transmission and a slider. The model tank made of polyacrylic resin was mounted on the slider and could be accelerated in the lateral direction up to about 1.0 G. As is shown in Fig. 8, the model tank, 0.20 m in diameter, consisted of a cylindrical part and an upper and a lower dome, which was similar to the LH_2 tank of the test vehicle with about 1/3.2 contraction dimension. There was a round bar along the center axis, which corresponded to the feed line in the real tank. In addition, as the devices for the damping of liquid motion, a conical baffle with round holes and a perforated cylinder could be equipped inside the tank.

In the present study, the main concern was focused on the unsteady deformation of the liquid surface in an

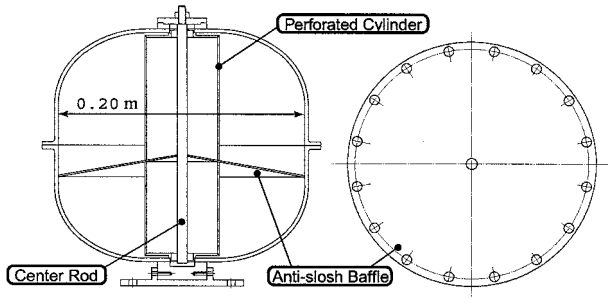

Fig. 8 The configuration of model tank and antislosh devices; $D = 0.20$ m

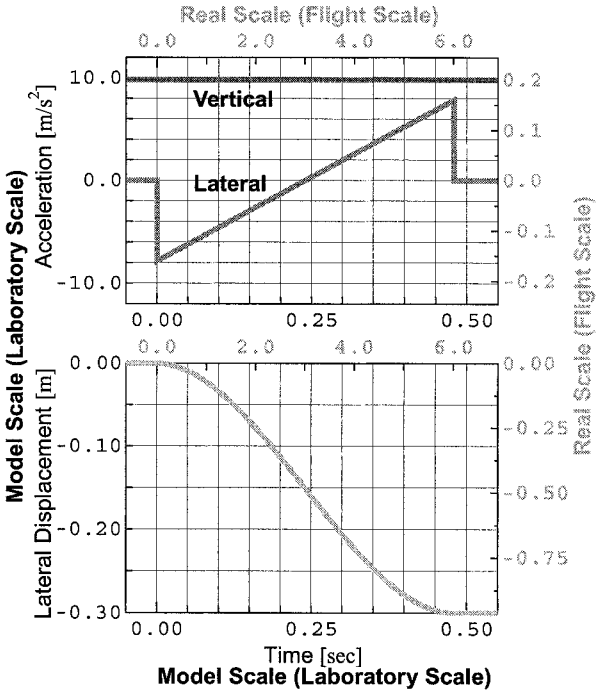

Fig. 9 Displacement of slider provided by a mechanical exciter for Case 1; lateral acceleration is 0.8 G at maximum.

environment where the vertical and lateral accelerations become comparable. As operating fluid, water H_2O at ambient temperature and normal pressure was utilized. The unsteady deformation of the liquid surface was observed with a high-speed camera through the transparent wall of the vessel. Figure 9 shows the displacement of the slider as a function of time, which was programmed and controlled by PC. In the experiments described in this section, the lateral acceleration provided by the mechanical exciter was varied linearly from −0.8 G to 0.8 G in 0.48 sec, while the vertical acceleration was fixed as 1.0 G, that is, the gravitational acceleration on the ground. If one assumes the similarity rule in terms of the Froude number between free-surface flows in the model tank and those in the real one, it is possible to transformed the liquid motion observed on the laboratory scale into that on the flight scale. In the present paper, only the case without the antislosh devices is reported.

Figure 10 shows the visualized flow field in the model

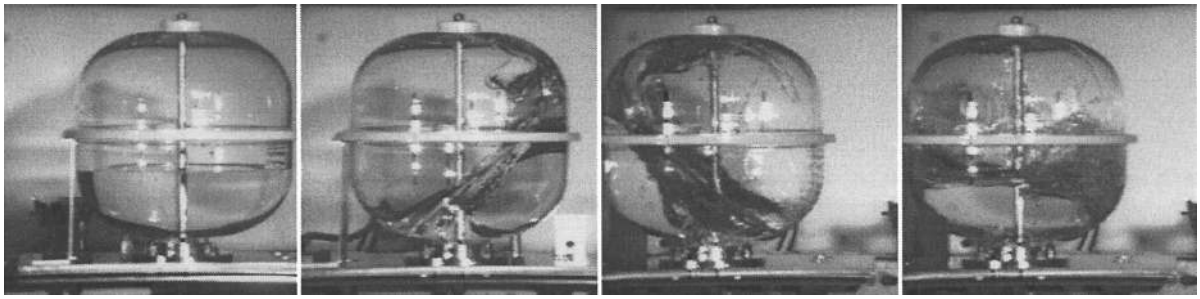

(a) 0.00 sec (b) 0.24 sec (c) 0.48 sec (d) 0.72 sec

Fig. 10 Sloshing in the model tank in Case 1. Without antislosh devices; visualized with a high-speed camera.; water as operating fluid; acceleration lateral: vertical = 0.8 : 1.0

tank. In this case, Case 1, the initial level of the liquid surface was set to be 0.08 m from the bottom, and the antislosh devices in the vessel, the baffle and cylinder, were removed. Since there is no blockage of the liquid motion except for the center rod, the liquid swayed once due to the inertial force to the right and swung back to the left. It was observed that the inclination of liquid surface became larger than the angular amplitude of the acceleration vector, the liquid wave reached the top of the tank and finally broke down. At the same time, a large amount of vapor was caught in the liquid wave, broke up into small bubbles and floated near the outlet port.

As long as the effects of viscosity and surface tension are allowed to be neglected, a similar flow can be realized in the subscale experiment. However the numerical investigation based on computational fluid dynamics, CFD, was still desired for more precise assessment, because it was practically impossible to reproduce the unsteady acceleration in the vertical direction on the ground and it was also difficult to carry out the experiments with a flight-scale tank containing cryogenic propellants.

4.2 Numerical assessment

Figure 11 shows the configuration of the computed domain which was similar to the model tank including the center rod. In this computation, water and air were used as the operating fluids. The liquid phase was supposed to be incompressible and the gaseous phase should obey the ideal gas equation. Initialy, the level of the liquid surface was as high as 0.08 m from the bottom and the temperature of each phase was given as 298.15 K, while the pressure was set to be about 1.0×10^5 Pa. The flow field was assumed to be plane symmetric and only the half around of the tank was solved with 50×90 stencils in a meridian section and 36 stencils in the circumferential direction. As the boundary condition on the surfaces of the tank liner and the center rod, both the non-slip and wetting conditions were imposed. The vertical and lateral accelerations were varied as shown in Fig. 9.

At first, the flow field of Case 1 was numerically simulated. In this case, the antislosh devices were removed. Figure 12 shows the time variation of the computed flow

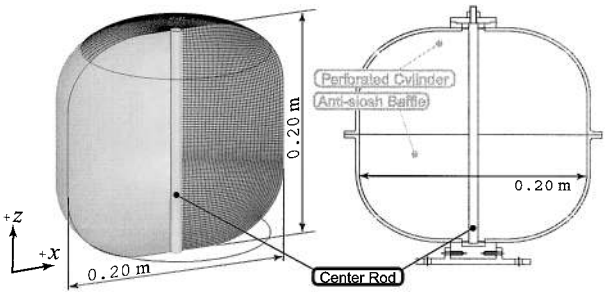

Fig. 11 Computed domain and grid system for the model tank with $50\times90\times36$ stencils

field. The liquid phase where the value of ϕ was positive was visualized by the dark-shaded region. Compared with the experimental results shown in Fig. 10, the cap of the wave at 0.24 sec, the liquid reaching the top at 0.48 sec and the following breakdown were clearly reproduced in the computation. It is therefore possible to say that CIP-LSM could capture the three-dimensional deformation of a liquid surface driven by inertial force and the numerical solution is thought to be fairly accurate. Even though bubbles and droplets smaller than the grid scale could not be captured because of the limited resolution, the liquid motion could be simulated with the developed code.

4.3 Further investigation

In the present study, the several configurations of antislosh devices in the tank were both experimentally and numerically investigated[15] to determine the optimum configuration for keeping the ullage gas away from the outlet port. Then, the flow fields in the real-scale tank were numerically simulated under the practical condition of acceleration. It was consequently suggested that the combination of a baffle plate and a perforated cylinder could be effective against the vapor suction before the re-ignition of the engine. It is expected to obtain more appropriate assessment on the dynamic behavior of liquid propellant in the space vehicles.

5. Conclusion

In this report, the sloshing problem in the propellant tank of a reusable rocket vehicle during ballistic flight was

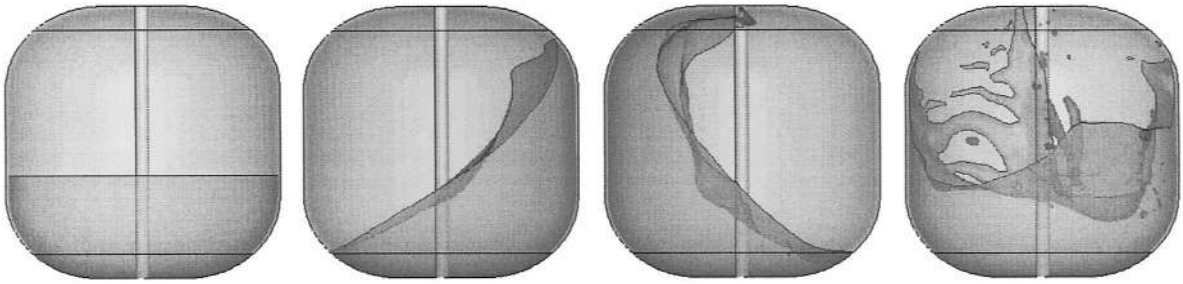

(a) 0.00 sec (b) 0.24 sec (c) 0.48 sec (d) 0.72 sec

Fig. 12 Sloshing in the model tank without antislosh devices; Case 3. Computed results corresponded to results for Case 1.

both experimentally and numerically investigated. In the experiment, the dynamic motions of the liquid surface in a model-scale tank driven by a mechanical exciter were successfully visualized. The observed flow field could be translated to the real-scale tank in accordance with the similarity rule in terms of the Froude number. Then, the flow fields observed in the experiment were numerically simulated with CIP-LSM. Although the bubbles and droplets smaller than the grid scale were not captured, as far as the main concern was focused on the surface deformation, fairly good agreement was obtained between the numerical results and the experimental data. However, in order to confirm the reliability of CIP-LSM, further investigation and more quantitative comparison are still required.

As was demonstrated in the present paper, the numerical analysis has the potential to provide helpful assessments for propellant management in a cost-effective manner. Indeed, the computational method of CIP-LSM is now under development. Further improvements and investigations are expected to clarify the various aspects of free-surface flows for the establishment of fluid-management technologies.

Acknowledgements

The authors express their great thanks to Prof. Kaneko in University of Tokyo who provided a lot of advice in the planning stage of the present experiment.

References

(1) Antar, B.N. and Nuotio-Antar, V.S., Fundamentals of Low Gravity Fluid Dynamics and Heat Transfer, (1993), CRC Press, ISBN 0-8493-8913-5.

(2) Inatani, Y., Naruo, Y. and Yonemoto, K., Concept and Preliminary Flight Testing of a Fully Reusable Rocket Vehicle, J. Spacecraft and Rockets, AIAA, Vol.38, No.1 (2001), pp.36–42.

(3) Himeno, T., Watanabe, T. and Konno, A., Numerical Analysis for Propellant Management in Liquid Rocket Tank, AIAA Paper 2001-3822, (2001).

(4) Himeno, T. and Watanabe, T., Numerical Analysis for Propellant Management in Rocket Tanks, AIAA J. Prop. &. Pwr., (to appear).

(5) Himeno, T. and Watanabe, T., Thermo-Fluid Management under Low-Gravity Conditions (2nd Report: Free-Surface Flows Driven by Surface Forces), Trans. JSME, Ser. B, (in Japanese), Vol.69, No.687 (2003), pp.2400–2407.

(6) Himeno, T. and Watanabe, T., Thermo-Fluid Management under Low-Gravity Conditions (1st Report: TCUP Method for the Analysis of Thermo-Fluid Phenomena), Trans. JSME, Ser. B, (in Japanese), Vol.69, No.678 (2003), pp.226–273.

(7) Yabe, T. and Wang, P.Y., Unified Numerical Procedure for Compressible and Incompressible Fluid, J. Phys. Soc. Japan, Vol.60 (1991), pp.2105–2108.

(8) Sussman, M., Smereka, P. and Osher, S., A Level Set Approach for Computing Solutions to Incompressible Two-Phase Flow, J. Comput. Phys., Vol.114 (1994), pp.146–159.

(9) Osher, S. and Fedkiw, R.P., Level Set Methods: An Overview and Some Recent Results, J. Comput. Phys., Vol.169 (2001), pp.463–502.

(10) Kunugi, T., Satake, S. and Ose, Y., Direct Numerical Simulation of Carbon-Dioxide Gas Absorption Caused by Turbulent Free Surface Flow, Int. J. Heat and Fluid Flow, Vol.22 (2001), pp.245–251.

(11) Youngs, D.L., Time-Dependent Multi-Material Flow with Large Fluid Distortion, Numerical Methods for Fluid Dynamics, edited by Morton, K.W. and Baines, M.J., (1982), p.273, Academic Press.

(12) Hirt, C.W. and Nichols, B.D., Volume of Fluid (VOF) Method for the Dynamics of Free Boundaries, J. Comput. Phys., Vol.39 (1981), p.201.

(13) Yabe, T. and Takei, E., A New Higher-Order Godnov Method for General Hyperbolic Equations, J. Phys. Soc. Japan, Vol.57 (1988), pp.2598–2601.

(14) Yabe, T., Xiao, F. and Utsumi, T., The Constrained Interpolation Profile Method for Multiphase Analysis, J. Comput. Phys., Vol.169 (2001), pp.556–593.

(15) Himeno, T., Nonaka, S., Naruo, Y., Inatani, Y. and Watanabe, T., Sloshing Prediction in the Propellant Tank of Reusable Rocket Vehicle, AIAA Paper 2003-4894.